Evaluating the use of Hyperspectral Imaging as Complementary Blood Sample Tests

Himar Fabelo[1], Raquel Leon[1], Samuel Ortega[1,2], Francisco Balea-Fernandez[3], Bernardino Clavo[4], Gustavo M. Callico[1], Ana Wagner[5,6]
[1]*Research Institute for Applied Microelectronics (IUMA), University of Las Palmas de Gran Canaria (ULPGC),* Las Palmas de Gran Canaria, Spain
[2]*Norwegian Institute of Food, Fisheries and Aquaculture Research (Nofima),* Tromsø, Norway
[3]*University of Las Palmas de Gran Canaria (ULPGC),* Las Palmas de Gran Canaria, Spain
[4]*Research Unit, Dr. Negrín University Hospital, Instituto de Investigación Sanitaria de Canarias (IISC),* Las Palmas de Gran Canaria, Spain
[5]*Research Institute of Biomedical and Health Sciences (IUIBS), University of Las Palmas de Gran Canaria (ULPGC),* Las Palmas de Gran Canaria, Spain
[6]*Department of Endocrinology and Nutrition, Complejo Hospitalario Universitario Insular Materno-Infantil,* Las Palmas de Gran Canaria, Spain
hfabelo, slmartin, sortega@iuma.ulpgc.es, fbalea@cop.es, bernardinoclavo@gmail.com, gustavo@iuma.ulpgc.es, ana.wagner@ulpgc.es

***Abstract*— Many diseases can be diagnosed by blood sample tests using automated analyzers. Novel imaging techniques, like Hyperspectral (HS) Imaging (HSI), are arising as potential tools for this purpose, offering quick and cost-effective approaches. In this paper, a methodology to use HS microscopic data of blood plasma samples to identify potential spectral biomarkers (SBs) and then quantify them in HS macroscopic data is presented. This quantification was performed using spectral unmixing algorithms. Finally, the abundance of each potential SB was correlated with each one of the blood test variable levels with and without removing outliers. Results found several statistically significant correlations ($p - value < 0.05$) and a highly significant correlation ($p - value < 0.01$) with the *creatinine* variable. These preliminary results show the potential of HSI sensors for performing quick and cost-effective blood sample tests.**

Keywords—Hyperspectral Imaging; Spectral Unmixing; Blood tests; Spectral Biomarkers; Hyperspectral Microscopy.

I. INTRODUCTION

Blood sample tests are one of the most common types of medical tests, having many applications, such as assessing the general state of health of a subject, checking for infections, evaluating certain organs functioning (liver, kidney,…), or screening for certain genetic conditions and diseases [1]. Commonly, a blood test is conformed of three main tests: a *complete blood count (CBC)*, a *basic metabolic panel (BMP)*, and a *lipoprotein panel*.

The CBC has the main goal of measuring the volume of blood cells (white blood cells, red blood cells and platelets) and their characteristics, allowing the evaluation of the overall health as well as checking for blood diseases and disorders, such as anemia, infections, clotting problems, blood cancers, or immune systems disorders [2]. The BMP, also called *blood chemistry test*, is in charge of measuring different chemicals in the blood (usually in plasma), such as glucose levels, calcium, and electrolyte balance, including also the liver and kidney function [2]. The lipoprotein panel is a blood test that provides information about the different types of triglycerides (fats) and cholesterol in blood, helping to evaluate the risk of coronary heart disease and other medical diseases [2].

Currently, automated hematology analyzers are employed to perform this analysis. However, nowadays, imaging technologies and processing algorithms are being investigated to provide rapid and cost-effective analysis of blood samples. In this sense, hyperspectral (HS) imaging (HSI) is arising as a promising alternative to conventional RGB (red, green, and blue) imaging modality for this purpose. HSI is a non-invasive and label-free technique that combines spectroscopy and conventional imaging methods to obtain both spatial and spectral information of the recorded scene [3]. Conventional RGB imaging captures three diffuse Gaussian spectral channels within the visible spectrum (~400–700 nm). On the contrary, HSI is able to capture spectral information within and beyond the human eye capabilities, measuring the reflected or absorbed radiance of light at specific wavelength of the material being recorded. HS sensors capture a large number of continuous spectral channels, conforming in each pixel of the image a vector of radiance values, the so-called *spectral signature* [3].

HSI has been investigated during many years in different fields [4]. In the medical field, HSI has been studied in the literature for several different applications like oncology [5], [6], gastroenterology [7], computational pathology [8], dermatology [6], [9], and many others [10]. Particularly, for the analysis of blood samples, Li *et al.* explored the feasibility of using HS microscopy in the 550-1000 nm spectral range for red blood cell counting, employing the combined spatial and spectral information [11]. The same group also employed HSI for the identification and extraction of the morphological features of leukocytes in blood smear samples [12]. Additionally, Verebes *et al.* proposed a method to identify red blood cells, white blood cells and neutrophils without performing a prior sample preparation using stains and HSI in the 400-1000 nm spectral range [13]. The use of unstained samples could lead to cost and time reduction in the blood sample preparations. Other studies have employed Raman spectroscopy for analyzing erythrocytes, leucocytes, platelets, plasma, and whole blood [14]. Additionally, NIR (near-infrared) spectroscopy have been studied for the analysis blood [15]. Particularly, Henn et al. used infrared spectroscopy in the range between 1000 to 2500 nm targeting hemodialysis monitoring, measuring glucose, lactate, phosphate and creatinine [16]. These studies reveal the potential of spectroscopy for measuring blood components. However, to the best of our knowledge, there are no studies in the literature that uses HSI in the VNIR (visual and near-infrared) range (400-1000 nm) to analyze blood plasma samples.

In this work, the use of HSI is evaluated for demonstrating its potential to perform quick and cost-effective blood sample tests, particularly in blood plasma. Previous works of this group have employed HSI microscopy to develop a methodology for identifying potential spectral biomarkers (SBs) in blood plasma samples for Alzheimer's disease detection [17]. In this case, the collected blood plasma samples are employed to perform a correlation analysis between the possible SBs, found in a subset of 10 HS microscopic images, and their abundances in the remaining 74 HS macroscopic images, and the different variable levels of the blood tests performed to the subjects included in the study, especially in the BMP and the lipoprotein panel.

2021 XXXVI Conference on Design of Circuits and Integrated Systems (DCIS) | 978-1-6654-2116-4/21/$31.00 ©2021 IEEE | DOI: 10.1109/DCIS53048.2021.9666164

II. Materials and Methods

This section will present in detail the materials employed to generate the HSI datasets of blood plasma samples, as well as the methods followed to extract the potential SBs and performing the correlation with the blood test variables. Fig. 1 shows the block diagram of the proposed methodology that will be explained in the next subsections.

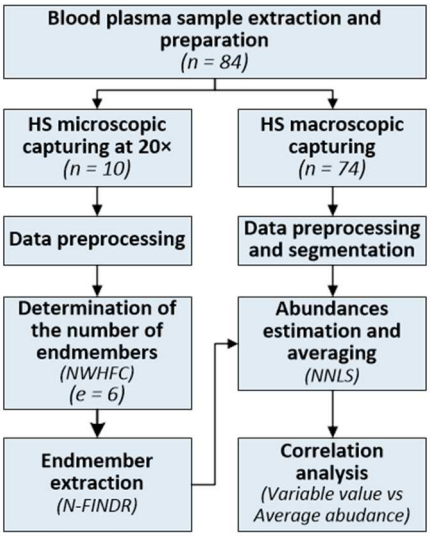

Fig. 1. Block diagram of the proposed methodology followed in this work.

A. Participant Recruitment and Sample Collection

Originally, the participants involved in the study were divided into two groups (control and case subjects), where the control group involved healthy subjects and the case group involved subjects with Alzheimer's disease [18]. In this study, all the participants have been included in the same group since the aim is to find a correlation between the spectral properties of the blood plasma HS images and the results of their respective blood tests.

Eighty-four subjects over 65 years old were recruited at the *Hospital Insular de Lanzarote* (Canary Islands, Spain), the *Asociación de Alzheimer Gran Canaria* (Canary Islands, Spain) and the *Peritia et Doctrina* program (university program for students over 55 years) of the University of Las Palmas de Gran Canaria (ULPGC, Canary Islands, Spain). The study protocol and consent procedures were approved by the *Comité de Bioética* of *the Hospital Universitario de Gran Canaria Doctor Negrin* (2019-054-1). The data acquisition campaign was carried out from March 2019 to October 2019. The average age of the participants was 79.8±8.4, and 26.2% were men.

A fasting blood test was requested for all subjects, and sampling was avoided in acute situations, such as infections. Table I shows the mean and standard deviation values of all the variables measured in the blood tests and their corresponding missing values. Variables are divided depending on the blood test from which they were obtained. The blood sample for the later data acquisition was drawn into a tube that contained sodium citrate as anticoagulant. Centrifugation was performed to separate plasma from blood cells, and plasma was transferred to another tube and frozen at -21 ºC for transport to the HS data acquisition laboratory. More details about the procedure can be found at [17].

TABLE I. Average and standard deviation (SD) of the analytical variables of the study participants.

Variable [Total without missing values/Total]	Mean	SD
CBC		
Hemoglobin (g/dL) [79/84]	12.85	1.91
MCV (fL) [79/84]	91.15	4.32
MCH (pg) [79/84]	30.13	1.84
Platelets (10^3 µL) [80/84]	235.50	68.22
Leukocytes (10^3 µL) [80/84]	6.79	1.86
Neutrophils (10^3 µL) [80/84]	4.04	1.55
Lymphocytes (10^3 µL) [80/84]	1.91	0.79
Monocytes (10^3 µL) [80/84]	0.61	0.28
BMP		
Glucose (mg/dL) [81/84]	109.91	28.81
Creatinine (mg/dL) [78/84]	0.98	0.36
GF (CKD-EPI) (mL/min) [72/84]	64.80	20.21
Sodium (mEq/L) [77/84]	141.31	3.51
Potassium (mEq/L) [77/84]	5.03	4.75
ALT (IU/L) [76/84]	18.17	21.46
Lipoprotein Panel		
Cholesterol (total) (mg/dL) [72/84]	176.79	40.85
LDL Cholesterol (mg/dL) [64/84]	98.02	36.32

MCV: Mean Corpuscular Volume; MCH: Mean Corpuscular Hemoglobin; CKD-EPI: Chronic Kidney Disease Epidemiology Collaboration; GF: Glomerular Filtration ALT: Alanine Aminotransferase; LDL: Low Density Lipoproteins.

B. Hyperspectral Data Acquisition

HS data was captured employing two different acquisition systems for microscopic and macroscopic data recording.

The microscopic system was composed by a pushbroom HS camera (Hyperspec® VNIR A-Series from HeadWall Photonics, Fitchburg, MA, USA) coupled to an Olympus BX-53 microscope (Olympus, Tokyo, Japan) with a motorized scanning platform (Scanning Stage SCAN 130×85, Märzhäuser). This system captured spectral information in transmittance mode from 400 to 1000 nm with a spectral resolution of 2.8 nm and a spatial resolution of 1004 × 400 pixels, generating 826 spectral channels. At 20× magnification the pixel size was of 370 nm. This system has been employed in related previous works [17], [19]. Fig. 2.a and c show the setup employed for the microscopic data capturing, and a gray-scale representation of the captured HS image of the plasma drop, respectively.

The macroscopic system was formed by a Hyperspec® VNIR A-Series from HeadWall Photonics (Fitchburg, MA, USA). This camera can capture spectral information within the range 400-100 nm with a spectral resolution of 2.5 nm and a spatial resolution of 1600 pixels, generating 923 spectral channels. This system employs a scanning platform to obtain the second spatial dimension of the HS image. This system was able to record spectral information in transmittance mode by using a fiber optic backlight illuminator (QVABL 4x3, Dolan-Jenner, Boxborough, MA, USA) coupled to an halogen-based illumination system (MI-150 Fiber-Lite®, Dolan-Jenner, Boxborough, MA, USA) able to emit in the spectral rage from 400 to 2200 nm. HS images of the drop plasma samples captured with this system had a spatial resolution of 440 × 440 pixels. Fig. 2.b shows the setup employed for the macroscopic data capturing and Fig. 2.d shows the synthetic RGB representation of the HS image

of the plasma drop captured using this system and after performing a manual segmentation (black pixels correspond to the background of the drop mask).

Prior to the HS data acquisition, samples were defrosted at room temperature (~23 ºC) for 1 hour. A drop of plasma (~0.05 ml) was deposited on a microscope glass slide and dried during 24 hours at room temperature. Then, 10 of the samples were captured using the microscopic system, while the remaining 74 samples were captured using the macroscopic system.

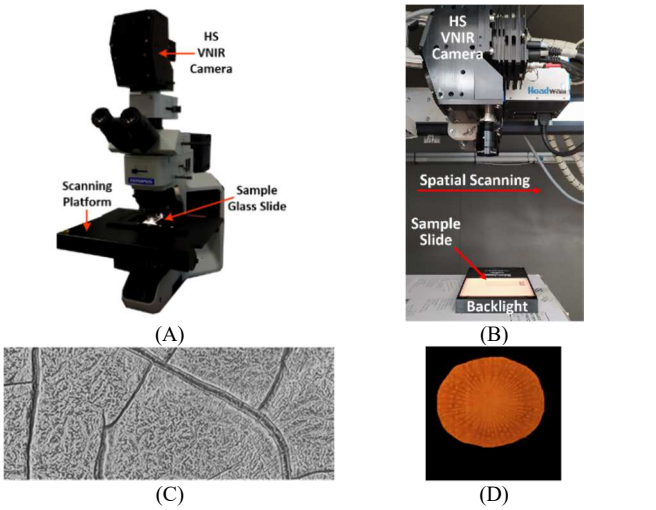

Fig. 2. Acquisition setups and example HS images employed in this work. (A) HS microscopic setup. (B) HS macroscopic setup. (C) Gray-scale representation of the HS image of the plasma drop obtained using the HS microscopic setup at 20× magnification. (D) RGB representation of the masked HS image of the plasma drop captured using the HS macroscopic setup.

C. Hyperspectral Data Pre-processing

Spectral data was preprocessed to reduce the dimensionality and noise, and to standardize the spectral signatures. In the first step, data was calibrated using white and dark reference images and computing Eq. 1, where CI_T is the calibrated image and RI_T the raw image in the transmittance mode. The white reference image (WI_T) was captured from a blank area of the microscope glass slide where no sample was located using the same illumination conditions as the sample was captured. The dark reference image (DI_T) was obtained turning off the illumination system (in the microscopic scenario) or covering the lens of the camera (in the macroscopic scenario). After the calibration step, data was converted from transmittance to absorbance values following Eq. 2, where CI_A is the calibrated image in absorbance mode.

$$CI_T = \frac{RI_T - DI_T}{WI_T - DI_T} \quad (1)$$

$$CI_A = -\log_{10}(CI_T) \quad (2)$$

Then, in the microscopic scenario, the first 56 bands and the last 126 bands were removed due to the low performance of the sensor in these spectral channels. Additionally, a decimation procedure was performed selecting one band for every 5 neighbor bands. This was motivated due to the high spectral resolution of the camera that produced high redundancy in the spectral information. The final HS cube was composed by 128 spectral channels. Due to the differences in the HS camera specifications between the microscopic and macroscopic scenarios, a procedure to adjust the HS data from the macroscopic system to the 128 spectral channels selected for the microscopic system was performed. In this procedure, the most similar wavelengths (from the macroscopic data) to the 128 selected wavelengths (of the microscopic data) were selected. At the end, both HS images had 128 spectral channels coincident to the first decimal value of the wavelength. Finally, noise filtering based on a moving average algorithm was applied to the HS data. The lowpass filter had a filter coefficient of 5. Additionally, for the HS macroscopic dataset, each drop in the image was manually segmented as shown in Fig. 2.d.

D. Spectral Biomarkers Identification and Quantification

The procedure to extract the SBs from the HS microscopic data was previously presented in [17]. The proposed method was based on a spectral unmixing (SU) technique, commonly used in HSI applications [20]. This technique is based on the principle that, in a HS image, each pixel can be modeled as a mixture of pure elements that are weighted and combined to form the spectral signature of such pixel [20]. Commonly, SU performs a blind source separation of pure spectral signatures (*endmembers*) from the mixed spectral signature, also computing the proportion (*abundance*) of each endmember in the mixed signature.

The procedure followed in this work to extract the endmembers from the microscopic data and compute their abundances in the macroscopic data is as follows. First, the HS microscopic dataset (composed by 10 images captured at 20× magnification from 10 different plasma samples) is merged in a single set of pixels. Then, the suitable number of endmembers in such set is determined, using the noise-whitened Harsanyi–Farrand–Chang (NWHFC) method [21], and the endmembers are extracted using the N-FINDR algorithm [22]. Once the optimal number of endmembers are extracted (six in our case) from the HS microscopic dataset, the abundances are estimated in each one of the images that compose the HS macroscopic dataset. This abundance estimation was performed using the non-negative least squares (NNLS) method [23], [24].

Finally, the average abundance for each endmember in each HS macroscopic image is computed using the drop mask previously created (Fig. 2.d).

E. Statistical Analysis

Pearson's Linear Correlation Coefficient ($rho_{pearson}$) and Spearman's Rank Correlation Coefficient ($rho_{spearman}$) were employed to evaluate the results obtained in this work. $rho_{pearson}$ was employed when both data vectors to be analyzed had a normal distribution, while $rho_{spearman}$ was employed when at least one of the vectors had a non-normal distribution. Data normality was evaluated using the Lilliefors test [25]. On the one hand, Eq. 3 shows the formula of the $rho_{pearson}$, where x and y are the two paired sample vectors $\{(x_1, y_1), \dots, (x_n, y_n)\}$, n is the sample size, and $\bar{x}$ and $\bar{y}$ are the sample means as shown in Eq. 4. On the other hand, the $rho_{spearman}$ is computed as presented in Eq. 5, where d is the difference between the ranks of the two paired sample vectors (Eq. 6) and n is the sample size.

The values of the correlation coefficient are in the range [-1,1], where -1 and +1 indicate perfect negative and positive correlation, respectively, while zero indicates no correlation between the data. Moreover, a two-tailed test at the 5% significance level was performed to compute the *p-values* for testing the alternative hypothesis that the correlation between the two vectors is not zero. Therefore, *p-values* lower than 0.05 are considered statistically significant.

$$rho_{pearson} = \frac{\sum_{i=1}^{n}(x_i - \bar{x})(y_i - \bar{y})}{\sqrt{\sum_{i=1}^{n}(x_i - \bar{x})^2}\sqrt{\sum_{i=1}^{n}(y_i - \bar{y})^2}} \quad (3)$$

$$\bar{x} = \frac{1}{n}\sum_{i=1}^{n} x_i \; ; \bar{y} = \frac{1}{n}\sum_{i=1}^{n} y_i \quad (4)$$

$$rho_{spearman} = 1 - \frac{6\sum_{i=1}^{n} d_i^2}{n(n^2-1)} \quad (5)$$

$$d_i = rg(x_i) - rg(y_i) \quad (6)$$

III. Experimental Results

This section will describe the correlations between the abundances of the potential SBs found in the HS macroscopic images and the blood test variables of the subjects.

A. Potential Spectral Biomarkers Identification

Fig. 3 shows the six endmembers found in the HS microscopic dataset. The different potential SBs have different characteristics. For example, SB6 has a clear peak of absorbance in ~510 nm, while the peak in SB2 is presented in ~580 nm. Moreover, SB3 has high absorbance contributions in the range between 650 to 900 nm, while SB1 and SB4 present high absorbance values in the entire spectral range.

B. Correlation Results Without Removing Outliers

As a first approach, the average abundance for each SB was correlated with the complete set of variables available from the blood tests. Missing values were not considered in the correlation computation. Fig. 4.A shows these correlations. Variables and SBs marked with (₸) had non-normal distributions, so rho values are obtained using the Spearman's method. Results marked with (*) and (¥) were found statistically significant ($p - value < 0.05$) and highly statistically significant ($p - value < 0.01$), respectively.

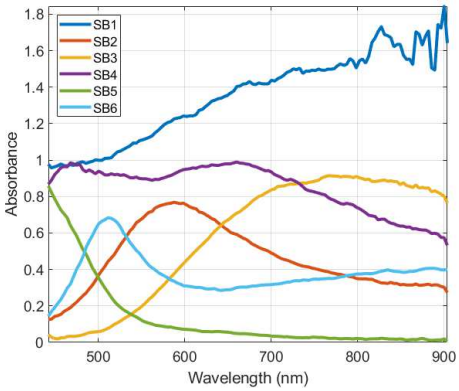

Fig. 3. Potential SBs identified in the HS microscopic images using the proposed method.

All the statistically significant results have a weak positive (or negative) correlation ($0.20 < rho < 0.39$). SB6 has a positive correlation with *hemoglobin* ($[rho = 0.280; p - value = 0.020]$) and *ALT* ($[rho = 0.245; p - value = 0.048]$), and a negative correlation with *neutrophils* ($[rho = -0.286; p - value = 0.016]$) and *monocytes* ($[rho = -0.285; p - value = 0.017]$). SB5 has a negative correlation with *neutrophils* ($[rho = -0.276; p - value = 0.021]$) and *monocytes* ($[rho = -0.291; p - value = 0.015]$). Finally, SB4 has a highly statistically significant positive correlation with *creatinine* ($[rho = 0.359; p - value = 0.003]$.

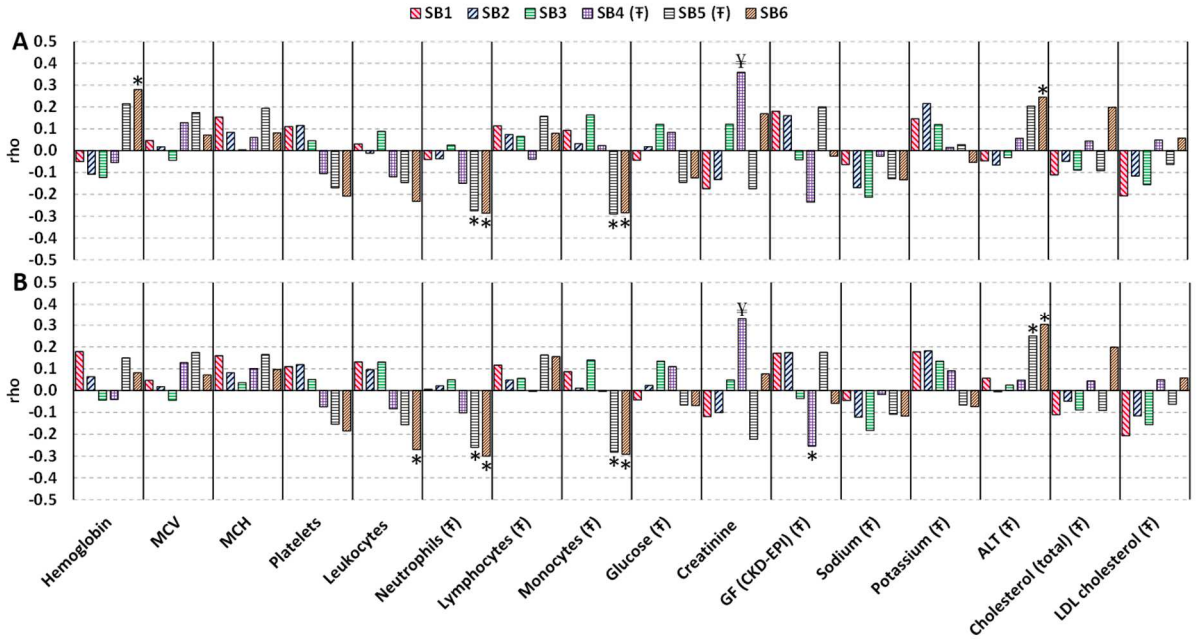

Fig. 4. Correlation results between the average abundances of each potential spectral biomarker and the different blood test variable levels. (A) Results obtained before removing outliers in each blood test variable set independently. (B) Results obtained after removing outliers. (₸) Indicates the variables and SBs with non-normal distributions, so rho values are obtained using the Spearman's method. (*) Indicates statistically significant correlation ($p - value < 0.05$). (¥) Indicates highly statistically significant correlation ($p - value < 0.01$). Zero *rho* values represent no correlation, while -1 and +1 represents perfect negative and positive correlations, respectively.

Fig. 5 shows the scatterplots of the correlation results obtained for the previously commented correlations. In some cases (especially in the *hemoglobin, monocytes, creatinine,* or *ALT* variable) there are outliers in the variable levels that could bias the results obtained in the correlation analysis. For this reason, this analysis was performed again after removing outliers in the blood test variable levels independently.

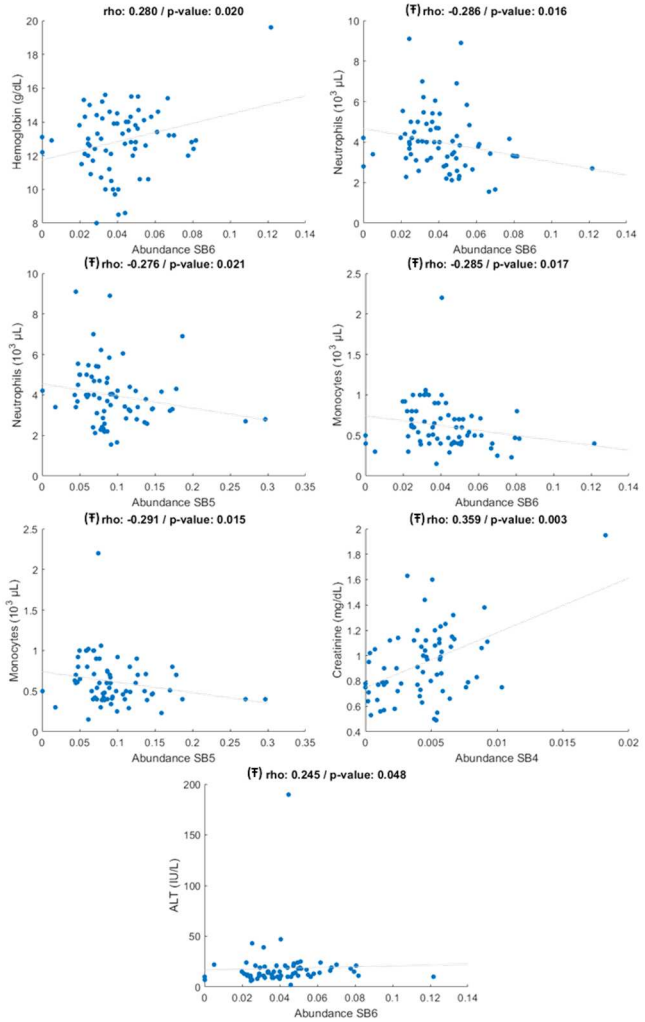

Fig. 5. Scatterplot of the relevant correlation results without removing outliers. (₮) Indicates the variables and SBs with non-normal distributions, so rho values are obtained using the Spearman's method.

C. *Correlation Results After Removing Outliers*

Considering the previous results where outliers can produce a bias in the correlation results, a procedure to identify and remove the outliers in the blood test variable levels was performed. Outliers were detected using the Interquartile Range (IQR) methodology. Then, outlier values were not employed to compute the correlation.

Fig. 4.B shows the results of this approach where the outliers have been removed from the dataset. It is worth noticing that in this case, the SB6 correlation with *hemoglobin* in the previous results are now not included here. In this case, SB5 still has a negative correlation with *neutrophils* ($[rho = -0.260; p - value = 0.032]$) and *monocytes* ($[rho = -0.282; p - value = 0.018]$), and also a positive correlation with *ALT* ($[rho = -0.251; p - value = 0.049]$). SB6 has a negative correlation with total *leukocytes* ($[rho = -0.271; p - value = 0.024]$), *neutrophils* ($[rho = -0.301; p - value = 0.013]$), and *monocytes* ($[rho = -0.292; p - value = 0.015]$). Moreover, SB6 has a positive correlation *ALT* variable ($[rho = 0.304; p - value = 0.016]$).

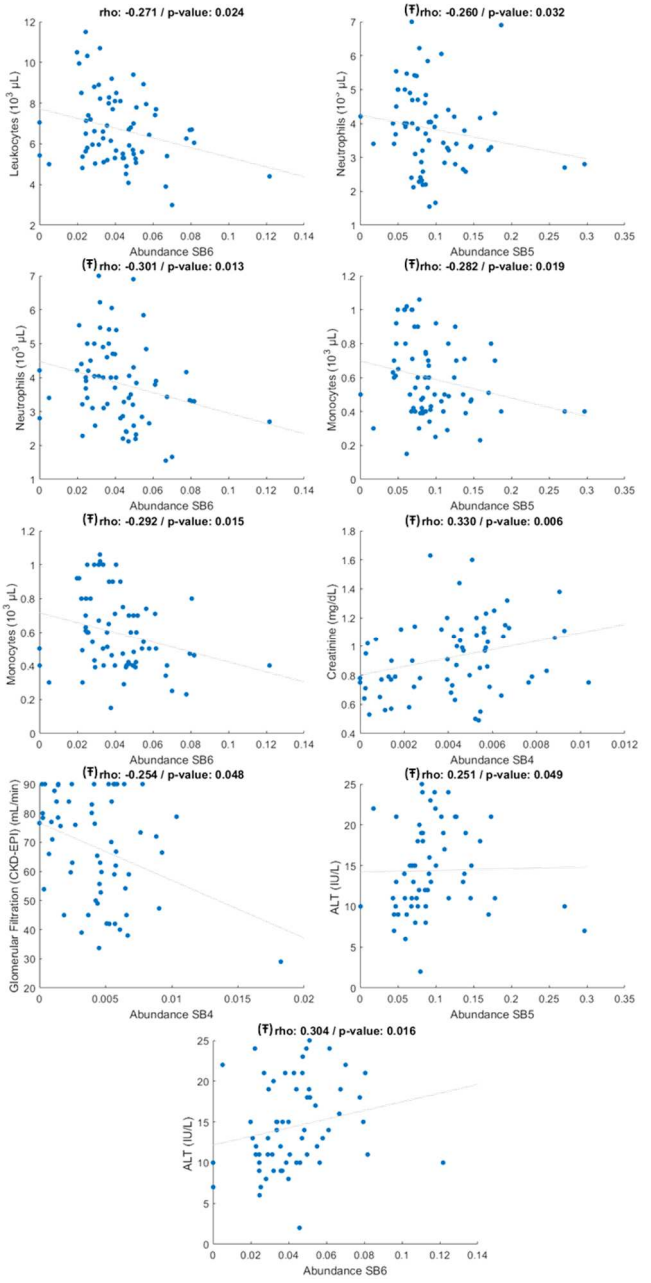

Fig. 6. Scatterplot of the relevant correlation results after removing outliers. (₮) Indicates the variables and SBs with non-normal distributions, so rho values are obtained using the Spearman's method.

Finally, in these results, SB4 has a highly statistically significant positive correlation with *creatinine* ($[rho = 0.330; p - value = 0.006]$) and a statistically significant negative correlation with estimated *glomerular filtration rate* ($[rho = -0.254; p - value = 0.048]$). The *glomerular filtration rate* is computed considering the *creatinine* level and other variables of the subject, like the age, sex, or ethnicity. Therefore, this could be the reason because there is an opposite correlation between these two variables with SB4. Fig. 6 represents the scatterplots of the most relevant correlation results generated in this experiment.

IV. CONCLUSIONS

This paper presents a preliminary study to assess the validity of HSI as a potential tool for blood sample tests. The work is based on previous methodology presented in [17] to extract potential SBs from HS microscopic images of blood plasma samples. Ten plasma samples from ten different subjects were used to identify six SBs. Then, these SBs were quantified in 74 HS macroscopic HS images of the entire blood plasma drop using an abundance estimation algorithm. Finally, these abundance values were correlated with the different blood test variable levels with and without removing outliers in the dataset.

The proposed methodology shows, as a proof of concept, that several SBs have statistically significant correlation with some variables. This is particularly relevant in the case of the BMP variables (*creatinine*, *glomerular filtration,* and *ALT*) that are commonly measured in plasma. However, rho values are generally low ($-0.35 < rho < 0.35$), indicating a weak correlation. Therefore, future work will aim to validate the proposed methodology including more subjects and performing the analysis not only in blood plasma but also in whole blood samples. Moreover, pure samples (e.g., pure creatinine) could be captured with the HS microscope to obtain its pure spectral signature, which will then be quantified in the plasma samples using the proposed methodology. These proposed algorithms could be implemented onto high performance computing platforms to achieve real-time results. These further experiments will evaluate the potential of HSI as a future quick and cost-effective method for blood tests in the point-of-care setting, compared with traditional, more time-consuming, methods, which require preparation of the samples, consumables, and more expensive and less eco-friendly equipment.

ACKNOWLEDGMENT

This work has been also supported in part by the European Commission through the H2020-EU.3.1.4.2., European Project WARIFA (Watching the risk factors: Artificial intelligence and the prevention of chronic conditions) under Grant Agreement 101017385, and by the Spanish Government and European Union (FEDER funds) as part of support program in the context of TALENT-HExPERIA (HypErsPEctRal Imaging for Artificial intelligence applications) project, under contract PID2020-116417RB-C42. Additionally, this work was completed while Raquel Leon was beneficiary of a predoctoral grant given by the "Agencia Canaria de Investigacion, Innovacion y Sociedad de la Información (ACIISI)" of the "Consejería de Economía, Conocimiento y Empleo", which is part-financed by the European Social Fund (FSE) (POC 2014-2020, Eje 3 Tema Prioritario 74 (85%)).

REFERENCES

[1] NHS, "Blood tests - NHS." [Online]. Available: https://www.nhs.uk/conditions/blood-tests/. [Accessed: 06-Jun-2021].

[2] NIH, "Blood Tests | NHLBI, NIH." [Online]. Available: https://www.nhlbi.nih.gov/health-topics/blood-tests. [Accessed: 06-Jun-2021].

[3] M. Kamruzzaman and D.-W. Sun, "Introduction to Hyperspectral Imaging Technology," *Comput. Vis. Technol. Food Qual. Eval.*, pp. 111–139, Jan. 2016.

[4] M. J. Khan, H. S. Khan, A. Yousaf, K. Khurshid, and A. Abbas, "Modern Trends in Hyperspectral Image Analysis: A Review," *IEEE Access*, vol. 6. Institute of Electrical and Electronics Engineers Inc., pp. 14118–14129, 12-Mar-2018.

[5] M. Halicek, H. Fabelo, S. Ortega, G. M. Callico, and B. Fei, "In-vivo and ex-vivo tissue analysis through hyperspectral imaging techniques: Revealing the invisible features of cancer," *Cancers (Basel).*, vol. 11, no. 6, 2019.

[6] R. Leon *et al.*, "Non-Invasive Skin Cancer Diagnosis Using Hyperspectral Imaging for In-Situ Clinical Support," *J. Clin. Med.*, vol. 9, no. 6, p. 1662, Jun. 2020.

[7] S. Ortega *et al.*, "Use of Hyperspectral/Multispectral Imaging in Gastroenterology. Shedding Some–Different–Light into the Dark," *J. Clin. Med.*, vol. 8, no. 1, p. 36, Jan. 2019.

[8] S. Ortega, M. Halicek, H. Fabelo, G. M. Callico, and B. Fei, "Hyperspectral and multispectral imaging in digital and computational pathology: a systematic review [Invited]," *Biomed. Opt. Express*, vol. 11, no. 6, p. 3195, Jun. 2020.

[9] F. Vasefi, N. MacKinnon, and D. L. Farkas, "Hyperspectral and Multispectral Imaging in Dermatology," in *Imaging in Dermatology*, 2016.

[10] G. Lu and B. Fei, "Medical hyperspectral imaging: a review.," *J. Biomed. Opt.*, vol. 19, no. 1, p. 10901, 2014.

[11] Q. Li, M. Zhou, H. Liu, Y. Wang, and F. Guo, "Red Blood Cell Count Automation Using Microscopic Hyperspectral Imaging Technology," *Appl. Spectrosc.*, vol. 69, no. 12, pp. 1372–1380, Dec. 2015.

[12] Q. Li *et al.*, "Leukocyte cells identification and quantitative morphometry based on molecular hyperspectral imaging technology.," *Comput. Med. Imaging Graph.*, vol. 38, no. 3, pp. 171–178, 2014.

[13] G. S. Verebes, M. Melchiorre, A. Garcia-Leis, C. Ferreri, C. Marzetti, and A. Torreggiani, "Hyperspectral enhanced dark field microscopy for imaging blood cells.," *J. Biophotonics*, vol. 6, no. 11–12, pp. 960–967, 2013.

[14] C. G. Atkins, K. Buckley, M. W. Blades, and R. F. B. Turner, "Raman Spectroscopy of Blood and Blood Components," *Appl. Spectrosc.*, vol. 71, no. 5, pp. 767–793, May 2017.

[15] K. B. Beć, J. Grabska, and C. W. Huck, "Near-Infrared Spectroscopy in Bio-Applications," *Molecules*, vol. 25, no. 12, p. 2948, Jun. 2020.

[16] R. Henn, C. G. Kirchler, Z. L. Schirmeister, A. Roth, W. Mäntele, and C. W. Huck, "Hemodialysis monitoring using mid- and near-infrared spectroscopy with partial least squares regression," *J. Biophotonics*, vol. 11, no. 7, p. e201700365, Jul. 2018.

[17] H. Fabelo *et al.*, "Novel Methodology for Alzheimer's Disease Biomarker Identification in Plasma using Hyperspectral Microscopy," in *2020 35th Conference on Design of Circuits and Integrated Systems, DCIS 2020*, 2020.

[18] F. J. Balea-Fernandez *et al.*, "Analysis of Risk Factors in Dementia through Machine Learning," *J. Alzheimer's Dis.*, vol. 79, no. 2, 2021.

[19] S. Ortega *et al.*, "Hyperspectral Imaging for the Detection of Glioblastoma Tumor Cells in H&E Slides Using Convolutional Neural Networks," *Sensors*, vol. 20, no. 7, p. 1911, Mar. 2020.

[20] J. M. Bioucas-Dias *et al.*, "Hyperspectral unmixing overview: Geometrical, statistical, and sparse regression-based approaches," *IEEE J. Sel. Top. Appl. Earth Obs. Remote Sens.*, vol. 5, no. 2, pp. 354–379, 2012.

[21] C.-I. Chang and Q. Du, "Estimation of Number of Spectrally Distinct Signal Sources in Hyperspectral Imagery," *IEEE Trans. Geosci. Remote Sens.*, vol. 42, no. 3, pp. 608–619, Mar. 2004.

[22] M. E. Winter, "N-FINDR: an algorithm for fast autonomous spectral end-member determination in hyperspectral data," in *Imaging Spectrometry V*, 1999, vol. 3753, pp. 266–275.

[23] M. Velez-Reyes and S. Rosario, "Solving adundance estimation in hyperspectral unmixing as a least distance problem," in *IEEE International IEEE International IEEE International Geoscience and Remote Sensing Symposium, 2004. IGARSS '04. Proceedings. 2004*, vol. 5, pp. 3276–3278.

[24] R. Bro and S. De Jong, "A fast non-negativity-constrained least squares algorithm," *J. Chemom.*, vol. 11, no. 5, pp. 393–401, Sep. 1997.

[25] H. W. Lilliefors, "On the Kolmogorov-Smirnov Test for Normality with Mean and Variance Unknown," *J. Am. Stat. Assoc.*, vol. 62, no. 318, pp. 399–402, 1967.